

TRANSITING EXOPLANET MONITORING PROJECT (TEMP). IV. REFINED SYSTEM PARAMETERS,
TRANSIT TIMING VARIATIONS AND ORBITAL STABILITY OF THE TRANSITING PLANETARY SYSTEM
HAT-P-25

XIAN-YU WANG,¹ SONGHU WANG,^{2,3} TOBIAS C. HINSE,⁴ KAI LI,¹ YONG-HAO WANG,^{5,6} GREGORY LAUGHLIN,²
HUI-GEN LIU,⁷ HUI ZHANG,⁷ ZHEN-YU WU,^{5,6} XU ZHOU,^{5,6} JI-LIN ZHOU,⁷ SHAO-MING HU,¹ DONG-HONG WU,⁷
XI-YAN PENG,^{5,6} AND YUAN-YUAN CHEN⁸

- ¹*Shandong Provincial Key Laboratory of Optical Astronomy and Solar-Terrestrial Environment, Institute of Space Sciences, Shandong University, Weihai 264209, China*
²*Department of Astronomy, Yale University, New Haven, CT 06511, USA*
³*51 Pegasi b Fellow*
⁴*Korea Astronomy and Space Science Institute, Daejeon 305-348, Republic of Korea*
⁵*Key Laboratory of Optical Astronomy, National Astronomical Observatories, Chinese Academy of Sciences, Beijing 100012, China*
⁶*School of Astronomy and Space Science, University of Chinese Academy of Sciences, Beijing 101408, China*
⁷*School of Astronomy and Space Science and Key Laboratory of Modern Astronomy and Astrophysics in Ministry of Education, Nanjing University, Nanjing 210093, China*
⁸*Purple Mountain Observatory, Chinese Academy of Sciences, Nanjing 210008, China*

ABSTRACT

We present eight new light curves of the transiting extra-solar planet HAT-P-25b obtained from 2013 to 2016 with three telescopes at two observatories. We use the new light curves, along with recent literature material, to estimate the physical and orbital parameters of the transiting planet. Specifically, we determine the mid-transit times (T_C) and update the linear ephemeris, $T_{C[0]}=2456418.80996\pm 0.00025$ [BJD_{TDB}] and $P=3.65281572\pm 0.00000095$ days. We carry out a search for transit timing variations (TTVs), and find no significant TTV signal at the $\Delta T=80$ s-level, placing a limit on the possible strength of planet-planet interactions (TTV_G). In the course of our analysis, we calculate the upper mass-limits of the potential nearby perturbers. Near the 1:2, 2:1, and 3:1 resonances with HAT-P-25b, perturbers with masses greater than 0.5, 0.3, and 0.5 M_{\oplus} respectively, can be excluded. Furthermore, based on the analysis of TTVs caused by light travel time effect (LTTE) we also eliminate the possibility that a long-period perturber exists with $M_p > 3000 M_J$ within $a = 11.2$ AU of the parent star.

Keywords: planetary systems — planets and satellites: fundamental parameters — planets and satellites: individual (HAT-P-25b) — stars: fundamental parameters — stars: individual (HAT-P-25) — techniques: photometric

1. INTRODUCTION

Thousands of transiting exoplanets have opened up a wealth of opportunities to discern nuances of the planetary formation and evolution processes.

In favorable cases, the measurement of planetary radii using transit photometry, combined with follow-up Doppler velocimetry (RV) measurements to determine masses, can reveal the bulk densities of representatives from the host of newly discovered super-Earths, determining, in turn, whether they are likely to be predominantly gaseous, watery or rocky worlds. Moreover, RV observations taken during transit permit measurement of projected spin-orbital misalignment angles, λ , of the transiting planets (e.g., [Queloz et al. 2000](#); [Winn et al. 2005](#); [Addison et al. 2014](#); [Winn & Fabrycky 2015a](#); [Wang et al. 2018a](#)).

High-precision photometric follow-up observations not only can confirm the planetary interpretation of a transit-signal detection, but they can also contribute to improve the accuracy of the planet’s physical and orbital parameters ([Wang et al. 2018b](#)). Moreover, high-precision photometric follow-up enables TTV assessments (e.g., [Holman & Murray 2005](#); [Agol et al. 2005](#)), which offer the prospect of detecting dynamically interesting perturbers. The architectures of systems that contain hot Jupiters provide clues that can potentially distinguish between competing formation theories for hot Jupiters ([Batygin et al. 2016](#)) and can add to the knowledge of general statistical trends of multi-planetary systems (e.g., [Steffen et al. 2012](#); [Huang et al. 2016](#)). Moreover, high-precision multi-band transit photometry permits exploration of the atmospheric properties of close-in planets, notably conditions related to the presence and potentially the compositions of clouds and hazes (e.g., [Sing et al. 2016](#)). Hence, we initialized the Transiting Exoplanet Monitoring Project (TEMP, [Wang Y. et al. 2017](#)) to study dozens exoplanet systems which have a lack of follow-up observations and/or show interesting TTV signals. We refine their system parameters, and orbital ephemerides, and characterize their dynamical histories by collecting and analyzing high-precision photometric light curves.

The transiting hot Jupiter HAT-P-25b was discovered by [Quinn et al. \(2012\)](#) under the auspices of the HATNet project. The system comprises a G5 dwarf star and a hot Jupiter, which has a transit period of $P = 3.652836 \pm 0.000019$ days. The host star ($V=13.19$) has an effective temperature of $T=5500 \pm 80$ K and a mass of $1.010 \pm 0.032 M_{\odot}$. The mass and radius of the planet were found to be $0.567 \pm 0.022 M_J$ and $1.190^{+0.081}_{-0.056} R_J$. As one of the first targets in TEMP, the photometric characterization of HAT-P-25 relies primarily on

two transit measurements including one incomplete light curve (the two light curves are refitted in this work – see §3) in the discovery paper ([Quinn et al. 2012](#)). Furthermore, the mid-transit times of the light curves listed in the Exoplanet Transit Database¹ (ETD) show substantial deviations from the linear ephemeris provided by [Quinn et al. \(2012\)](#). As a consequence, follow-up observations are needed to consolidate the system parameters and to improve the overall characterization.

In this work, we present the first transit photometry of HAT-P-25b since the discovery paper, covering eight transits. These new transits, when combined with the published data from [Quinn et al. \(2012\)](#), allow us to refine the physical and orbital parameters. Based on the analysis of mid-transit times derived from all available follow-up light curves (eight from this work, and two from [Quinn et al. 2012](#)), we determine an updated linear ephemeris, as well as upper mass limits on potential nearby and long-term perturbers.

We proceed as follows. In § 2, we detail the observations and data reduction. An analysis of the resulting light curves is presented in § 3 and § 4 describes a dynamical analysis of this system, and places the assessment of HAT-P-25 into the broader context provided by the galactic planetary census, before segueing into the final section which contains a brief summary and overview.

2. OBSERVATIONS AND DATA REDUCTION

Between September 2013 and November 2016, we observed eight transits of HAT-P-25b with three telescopes at two different sites. Three of transits were observed with the 1-m telescope at the Weihai Observatory (WHOT; $122^{\circ}02'58.6''E$, $37^{\circ}32'09.3''N$) of the Shandong University in China, and others were observed with the 60 cm telescope and the 60/90 cm Schmidt telescope at Xinglong Station ($117^{\circ}34'30''E$, $40^{\circ}23'39''N$) of the National Astronomical Observatories of China (NAOC).

2.1. Weihai Observatory

Three Johnson V band transits of HAT-P-25b were obtained at Weihai Observatory in 2013, on September 25, October 17 and November 30. With a $2K \times 2K$ imaging array ($13.5 \times 13.5 \mu m \text{ pixel}^{-1}$), the telescope provides a field of view of $12' \times 12'$, and a pixel scale of $0.35'' \text{ pixel}^{-1}$. The full technical details of this telescope are given [Hu et al. \(2014\)](#).

In each run, exposure times were held fixed to avoid adverse systematic effects on the measurements of mid-transit times. The time on the telescope and CCD con-

¹ <http://var2.astro.cz/ETD/index.php>

Table 1. Log of Observations

Date (UTC)	Time (UTC)	Telescope	Filter	Number of exposures	Exposure time (second)	Airmass	Moon Phase	Distance ^a degree	Scatter ^a
2013 Sep 25	16:40:25-20:53:39	Weihai 1 m	V	221	50	1.02-1.16	0.00	26.00	0.0035
2013 Oct 17	14:58:49-18:32:24	Weihai 1 m	V	202	40	1.02-1.18	0.98	43.80	0.0053
2013 Nov 19 ^b	12:15:18-16:21:57	Xinglong 60/90 cm Schmidt	R	95	120	1.06-1.37	0.96	27.71	0.0030
2013 Nov 30	10:31:55-14:40:40	Weihai 1 m	V	229	50	1.02-1.59	0.09	160.20	0.0029
2015 Feb 04	10:56:25-15:02:29	Xinglong 60/90 cm Schmidt	R	136	80	1.04-1.92	0.99	170.00	0.0034
2016 Jan 17	11:07:08-15:29:06	Xinglong 60 cm	R	121	100	1.04-1.55	0.59	20.20	0.0027
2016 Jan 28 ^b	11:47:06-15:02:28	Xinglong 60/90 cm Schmidt	R	65	150	1.06-1.67	0.80	125.67	0.0039
2016 Nov 04	16:44:43-21:12:31	Xinglong 60/90 cm Schmidt	R	84	180	1.04-2.00	0.25	133.33	0.0020

^a Distance is the mean of the distance between the target and the moon on the sky during the observation. Scatter represents the RMS of the residuals from the best-fitting transit model.

^b Due to bad weather, the observations were interrupted, resulting in two partial transit light curves.

trol computers were GPS-synchronized at a one-minute cadence. The HJD time stamps in each FITS header log the mid-exposure time, and were logged from the synchronized system time following the UTC time standard. For the accurate timing studies presented later in this work, we converted the HJD time stamps in the UTC time standard to BJD time stamps valid in the TDB time standard. The precise time management techniques that we used are described in [Eastman et al. \(2010\)](#).

Using standard procedures, all data were debiased and flat-fielded. Aperture photometry was then obtained using the Source Extractor Software Package ([Bertin & Arnouts 1996](#)). Transit light curves were obtained using differential photometry. The choice of apertures and photometric comparison stars were adjusted manually in order to produce the lowest scatter among observations taken out of transit.

2.2. Xinglong Station, National Astronomical Observatory

Between 2013 November and 2016 November, four Johnson *R* band transits of HAT-P-25b were obtained with the 60/90 cm Schmidt telescope at Xinglong Station of the NAOC of China, and an additional transit was monitored with the R-band using the 60 cm telescope. The 60/90 cm Schmidt telescope is equipped with a 4K×4K CCD, which gives a 94' × 94' field of view with a pixel scale of 1.38'' pixel⁻¹. The 60 cm telescope is equipped with a 1K×1K CCD, which provides a 17' × 17' effective field of view with a pixel scale of 1.00'' pixel⁻¹. More instrumental details for these telescopes can be found in [Zhou et al. \(1999\)](#) and [Yang \(2009\)](#).

Table 2. Photometry of HAT-P-25

BJD _{TDB} ^a	Relative Flux	Uncertainty	Filter
2456561.199442	1.0018	0.0028	R
2456561.200288	1.0018	0.0028	R
2456561.201028	0.9954	0.0028	R
2456561.201881	0.9932	0.0028	R
2456561.202627	0.9954	0.0028	R
2456561.203472	1.0008	0.0028	R
2456561.204225	1.0008	0.0028	R
2456561.205068	0.9954	0.0028	R
2456561.205809	1.0014	0.0028	R
...

^a Time stamps throughout the paper have been converted to BJD_{TDB}.

Due to bad weather, the observations on Nov 19, 2013, and Jan 28, 2016, were interrupted, which resulted in two partial transit light curves.

We used the same strategy described in §2.1 to handle the data from the observations performed at Xinglong station. A detailed summary of observations is presented in Table 1. The resulting transit curves are listed in Table 2, and are shown in Figures 1 and 2.

3. LIGHT CURVE ANALYSIS

To re-estimate the global parameters, we employed Multi-EXOFAST² ([Eastman et al. 2013](#)), a speed-optimized suite of exoplanet model-fitting software writ-

² A description of the procedure can be found at <http://astrutils.astronomy.ohio-state.edu/exofast/>.

ten in IDL which can fit multiple follow-up transit light curves in different filter bands and multiple RV telescope data sets (Collins et al. 2017). The package is able to fit transit data and RVs simultaneously, which can improve the quality of both fit types and provide a clearer picture of the system under consideration (Eastman et al. 2013). In our treatment, each data set was first fitted separately to scale the uncertainties and to derive a preliminary best fit. Then, based on the Differential Evolution Markov Chain Monte Carlo (DE-MCMC; ter Braak 2006), the package was employed to carry out a global fit to all data sets. This permitted refinement of the best joint fit. Stellar parameters were calculated with the help of Torres relations (Torres et al. 2008). By using standard MCMC techniques to evaluate the posterior density, we determined robust uncertainty estimates for the parameters. As described in Eastman et al. (2013), a given Markov chain is considered to be converged when both the number of independent draws is greater than 1000 and the Gelman-Rubin statistic is less than 1.01 for all parameters. During fitting, Markov chains that satisfy these criteria six consecutive times are considered to be well-mixed.

For comparison purposes, we performed global fitting for three different incarnations of the joint data set. In the first incarnation, we used the eight new light curves obtained from this work in conjunction with the RVs from discovery work (a set we call “8 new light curves + RVs”). In the second incarnation we used the two extant light curves from the literature in conjunction with RVs from the discovery work (a set we call “2 literature light curves + RVs”). In the third incarnation we used Multi-EXOFAST to deal with all ten above-mentioned light curves in three different filter bands and the RVs from discovery work (a set we call “All light curves + RVs”). The parameters we used in order to initialize the fits are from Quinn et al. (2012). The results from the three different global fittings and their errors are presented in Table 3. After making a comparison between the fits (details can be seen in §4.1), we selected the parameters from the “All light curves + RVs” set as the best representation of the global parameters. The fitting results are shown in Figure 2.

With the best global parameters derived from the “All light curves + RVs” data set in hand, we applied the JKTEBOP routine³ (Southworth et al. 2004a; Southworth et al. 2004b), a fast procedure that can analyze light curves of detached eclipsing binaries and transiting extra-solar planetary systems. This allowed us

to accurately measure mid-transit times of the eight new light curves from this work and the two acquired from the discovery paper (Quinn et al. 2012). In the JKTEBOP fitting, we fixed all the parameters derived from previously global fitting and just considered the mid-transit times and baseline fluxes as free parameters for each light curve to float. Using Levenberg-Marquardt optimization, we derived mid-transit times. Furthermore, through comparing uncertainties generated with the residual-permutation algorithm and with Monte Carlo simulations (10,000 trials), we consistently chose the larger of the obtained uncertainties of mid-transit times to secure a conservative estimate. The mid-transit times derived using JKTEBOP are listed in Table 5.

4. RESULT AND ANALYSIS

4.1. System Parameters

Based on the analysis described in §3, the updated physical and orbital parameters for the HAT-P-25 system, along with their errors, are presented in Tables 3. The tables also include estimates stemming from the previous work (Quinn et al. 2012). The best-fitting model of transit and RV are shown in Figures 1 and 3.

The results of the three different global fits are mutually consistent. Moreover, compared with the quality of the parameters in the other two fittings, the “All light curves + RVs” fit indicates that the accuracy of 28 of the 46 parameters has improved; all important parameters were improved except stellar mass, effective temperature, metallicity, argument of periastron, planetary mass, ingress/egress duration (details can be seen in Table 3). Therefore, the result of the global fitting, the “All light curves + RVs” model, is regarded as the best global fitting result. Extrapolating from the RMS residuals of individual fits shown in Figure 2 and the observation logs, we can conclude that with more favorable sky conditions and with the use longer exposure times (in conjunction with appropriate defocusing) one might be able to obtain lower RMS⁴. We have also carried out a similar model calculation that retains only the *V/Sloani/R*-filter data. For that case, the planetary and stellar radius ratios R_P/R_* in each band were found to be within the radius measurement presented in Table 4. From this we conclude that the current data do not allow for differentiation between pass-band de-

³ Code is available in its entirety at <http://www.astro.keele.ac.uk/jkt/codes/jktebop.html>.

⁴ Because the light curves of ‘2013 Nov 19’ and ‘2016 Jan 28’ are partial, we performed a Pearson correlation analysis the corpus of data exclusive of these light curves. The Pearson correlation coefficient between exposure times and RMS is $r = -0.74$, whereas that between the moon-target distance and the RMS is $r = -0.36$.

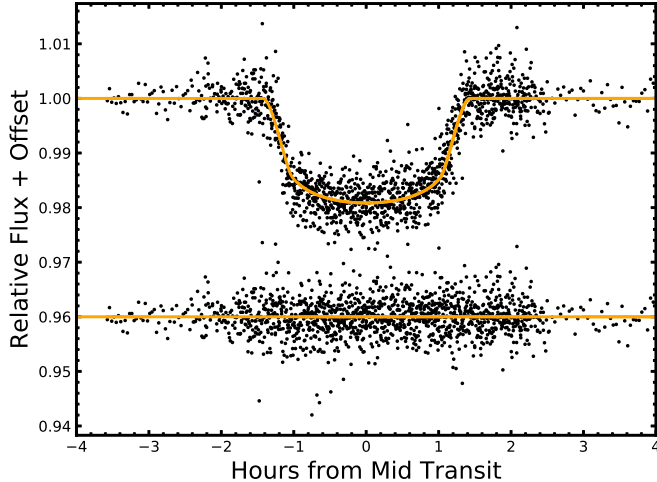


Figure 1. Combined photometry of HAT-P-25, shown as a function of orbital phase. To estimate the system parameters, we fit the combined light curves along with the radial velocity measurements (not shown). The best-fitting model to all of the data is plotted as solid orange line and the residuals (once the model has been removed) are shown in the lower part of the figure.

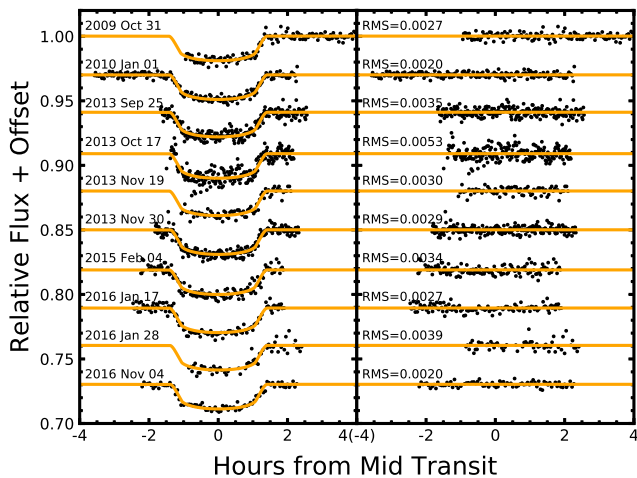


Figure 2. Light curves of the HAT-P-25b transit obtained in individual runs. The Top two light curves are from Quinn et al. (2012), and the bottom eight light curves belong to this work. Based on JKTEBOP code, the mid-transit times are estimated by analyzing these data. The best-fitting models, from the joint analysis of the RV data and the ensemble photometric light curves, are plotted as solid orange lines. The residuals of fits and their RMS errors from JKTEBOP are displayed on the right panel, in the same order as the light curves. For clarity, we make offset of light curves and residuals artificial. More details of each light curves can be seen in Table 1.

pendent radius measurements. In summary, our work provides the following updates to the characterization of the system provided in the discovery paper:

Given that the same RVs were used, it comes as no surprise that we find all Doppler velocimetric properties consistent with those of discovery work (Quinn et al. 2012). The RV parameters derived from our work are all in agreement with those from discovery work to within 0.61σ .

The transit parameters that we derive are all consistent with the discovery work, and all of the parameters other than the inclination have had their uncertainties reduced. Given that the identical stellar spectroscopic parameters were used here and in the discovery work, there is full consistency with Quinn et al. (2012).

Perhaps the most important update from our analysis is the significant improvement to the period, which stems from the use of a more extensive collection of mid-transit times (see the description in §4.2).

Based on the above, the unsurprising conclusion is that the physical and orbital parameters for HAT-P-25b agree with those of discovery work within the uncertainties.

4.2. Transit Timing

Mid-transit times, T_C , derived from each new and literature light curves, are listed in Table 5. To calculate an updated linear ephemeris, that can be employed to predict the transit time accurately and to analyze TTVs, we employed a weighted least square method to fit all ten mid-transit times (T_C) with a linear function of transit epoch number (E),

$$T_{C[E]} = T_{C[0]} + E \times P, \quad (1)$$

where $T_{C[E]}$ is the mid-transit time, $T_{C[0]}$ is mid-transit time of the reference epoch and P is period. The results are $T_{C[0]} = 2456418.80996 \pm 0.00025$ [BJD_{TDB}] and $P = 3.65281572 \pm 0.00000095$ days. This fit has a reduced $\chi^2 = 1.60$ (RMS=80 s). The new orbital period of HAT-P-25b is twenty times more precise than the period reported in discovery work, an improvement enabled by our long-term series of follow-up observations. We chose the middle epoch within our observations as the reference epoch to minimize covariance with the orbital period. Furthermore, the updated linear ephemeris not only fits the ten mid-transit times in this work well ($\chi^2_{\text{reduced}} = 1.60$), but also fits the data of ETD well, giving $\chi^2_{\text{reduced}} = 9.76$ whereas the linear ephemeris of discovery work gives $\chi^2_{\text{reduced}} = 130.45$. Figure 4 displays the deviation of mid-transit times for HAT-P-25b from our updated linear ephemeris, showing no significant timing variations at a level above 80s.

Given the lack of significant timing variations, we can calculate the upper mass-limits of potential nearby perturbers (§4.3) and long-term perturbers (§4.4). The

determinations are based on the analysis of TTVs caused by planet-perturber interaction (TTV_G) and the perturber-induced stellar barycentric movement (known as light travel time effect, TTV_{LTTE}) respectively.

Table 3. System parameters for HAT-P-25

Parameter	Units	Priors ^a	8 new LCs + RVs	2 literature LCs + RVs	All light curves + RVs	Quinn et al. (2012) ^b agreement(σ) ^c
Stellar Parameters:						
M_*	Mass (M_\odot)	1.010 ± 0.032	$1.018^{+0.055}_{-0.053}$	$1.007^{+0.054}_{-0.052}$	$1.012^{+0.053}_{-0.051}$	1.010 ± 0.032 0.03
R_*	Radius (R_\odot)	$0.947^{+0.044}_{-0.041}$	$0.930^{+0.039}_{-0.038}$	$0.926^{+0.043}_{-0.041}$	0.919 ± 0.034	$0.959^{+0.054}_{-0.037}$ 0.80
L_*	Luminosity (L_\odot)	...	$0.731^{+0.086}_{-0.076}$	$0.692^{+0.088}_{-0.077}$	$0.705^{+0.076}_{-0.070}$	0.75 ± 0.10 0.36
ρ_*	Density (cgs)	...	$1.79^{+0.19}_{-0.17}$	$1.79^{+0.22}_{-0.19}$	$1.84^{+0.17}_{-0.15}$
$\log(g_*)$	Surface gravity (cgs)	4.48 ± 0.04	4.509 ± 0.028	4.508 ± 0.032	$4.516^{+0.026}_{-0.025}$	4.48 ± 0.04 0.76
T_{eff}	Effective temperature (K)	5500 ± 80	5540^{+79}_{-78}	5476 ± 80	5519^{+78}_{-76}	5500 ± 80 0.17
[Fe/H]	Metallicity	0.31 ± 0.08	$0.286^{+0.079}_{-0.080}$	$0.314^{+0.080}_{-0.078}$	0.294 ± 0.080	0.31 ± 0.08 0.14
Planetary Parameters:						
e	Eccentricity	0.032 ± 0.022	$0.024^{+0.022}_{-0.015}$	$0.025^{+0.022}_{-0.016}$	$0.023^{+0.022}_{-0.014}$	0.032 ± 0.022 0.29
ω_*	Argument of periastron (degrees)	271 ± 117	-74^{+50}_{-16}	286^{+46}_{-15}	287^{+52}_{-17}	271 ± 117 0.14
P	Period (days)	3.652836 ± 0.000019	$3.6528140^{+0.0000017}_{-0.0000018}$	$3.6528153^{+0.0000080}_{-0.0000079}$	$3.65281514^{+0.00000076}_{-0.00000075}$	3.652836 ± 0.000019 1.10
a	Semi-major axis (AU)	0.04658 ± 0.000776	0.04669 ± 0.00082	0.04653 ± 0.00082	$0.04660^{+0.00081}_{-0.00080}$	0.0466 ± 0.0005 0.00
M_P	Mass (M_J)	...	$0.571^{+0.023}_{-0.022}$	0.568 ± 0.022	$0.569^{+0.023}_{-0.022}$	0.567 ± 0.022 0.06
R_P	Radius (R_J)	$1.190^{+0.081}_{-0.056}$	$1.154^{+0.057}_{-0.056}$	$1.143^{+0.063}_{-0.060}$	1.135 ± 0.048	$1.190^{+0.081}_{-0.056}$ 0.75
ρ_P	Density (cgs)	0.42 ± 0.070	$0.462^{+0.067}_{-0.057}$	$0.471^{+0.075}_{-0.064}$	$0.483^{+0.059}_{-0.051}$	0.42 ± 0.070 0.73
$\log(g_P)$	Surface gravity	...	$3.027^{+0.038}_{-0.037}$	3.032 ± 0.042	$3.039^{+0.033}_{-0.032}$	$3.0^{+0.04}_{-0.06}$ 0.76
T_{eq}	Equilibrium Temperature (K)	...	1191^{+28}_{-26}	1177^{+30}_{-29}	1182 ± 25	1202 ± 36 0.46
Θ	Safronov Number	...	$0.0454^{+0.0025}_{-0.0023}$	$0.0458^{+0.0027}_{-0.0025}$	$0.0461^{+0.0023}_{-0.0021}$	0.044 ± 0.003 0.57
$\langle F \rangle$	Incident flux ($10^9 \text{ erg s}^{-1} \text{ cm}^{-2}$)	...	$0.457^{+0.044}_{-0.039}$	$0.436^{+0.046}_{-0.041}$	$0.442^{+0.039}_{-0.036}$	0.472 ± 0.58 0.05
RV Parameters:						
$e \cos \omega_*$...	$0.0060^{+0.0069}_{-0.0061}$	$0.0064^{+0.0068}_{-0.0062}$	$0.0062^{+0.0068}_{-0.0062}$	0.008 ± 0.012 0.13
$e \sin \omega_*$...	$-0.022^{+0.020}_{-0.024}$	$-0.023^{+0.020}_{-0.024}$	$-0.020^{+0.019}_{-0.024}$	-0.020 ± 0.034 0.00
T_P	Time of periastron (BJD _{TDB})	...	$2455200.77^{+0.51}_{-0.17}$	$5200.77^{+0.47}_{-0.16}$	$5200.78^{+0.53}_{-0.18}$
K	RV semi-amplitude (m/s)	74.3 ± 2.4	74.5 ± 1.4	74.5 ± 1.4	74.5 ± 1.4	74.3 ± 2.4 0.14
$M_P \sin i$	Minimum mass (M_J)	0.56683 ± 0.026307	$0.571^{+0.023}_{-0.022}$	0.567 ± 0.022	$0.569^{+0.023}_{-0.022}$
M_P/M_*	Mass ratio	...	0.000536 ± 0.000014	0.000538 ± 0.000014	0.000537 ± 0.000014
γ	Systemic velocity (m/s)	...	1.1 ± 1.0	1.1 ± 1.0	1.0 ± 1.0
$\dot{\gamma}$	RV slope (m/s/day)	...	$-0.046^{+0.045}_{-0.046}$	-0.047 ± 0.046	$-0.047^{+0.045}_{-0.046}$
Primary Transit Parameters:						
R_P/R_*	Radius of planet in stellar radii	...	$0.1275^{+0.0013}_{-0.0014}$	0.1269 ± 0.0015	0.1269 ± 0.0011	0.1275 ± 0.0024 0.23
a/R_*	Semi-major axis in stellar radii	$10.46^{+0.38}_{-0.55}$	$10.80^{+0.37}_{-0.35}$	$10.81^{+0.42}_{-0.40}$	$10.90^{+0.33}_{-0.31}$	$10.46^{+0.38}_{-0.55}$ 0.9

Table 3 continued

Table 3 (continued)

Parameter	Units	Priors ^a	8 new LCs + RVs	2 literature LCs + RVs	All light curves + RVs	Quinn et al. (2012) ^b agreement(σ) ^c
u_1	linear limb-darkening coeff ^d	0.373 ± 0.014	... ^e	0.3287
u_2	quadratic limb-darkening coeff ^d	$0.2473^{+0.0077}_{-0.0084}$... ^e	0.3039
i	Inclination (degrees)	87.6 ± 0.5	$88.09^{+0.53}_{-0.40}$	$88.00^{+0.62}_{-0.48}$	$88.22^{+0.45}_{-0.36}$	87.6 ± 0.5
b	Impact Parameter	$0.45607^{+0.068411}_{-0.066586}$	$0.369^{+0.067}_{-0.096}$	$0.386^{+0.079}_{-0.11}$	$0.347^{+0.061}_{-0.082}$	$0.456^{+0.073}_{-0.098}$
δ	Transit depth	0.016526 ± 0.000612	0.01626 ± 0.00035	$0.01610^{+0.00038}_{-0.00037}$	0.01610 ± 0.00027	...
T_{FWHM}	FWHM duration (days)	...	0.10258 ± 0.00055	$0.10178^{+0.00085}_{-0.00086}$	$0.10235^{+0.00048}_{-0.00047}$...
τ	Ingress/egress duration (days)	...	0.0152 ± 0.0012	$0.0153^{+0.0015}_{-0.0013}$	$0.01485^{+0.00094}_{-0.00091}$	0.0163 ± 0.0018
T_{14}	Total duration (days)	0.1174 ± 0.0017	0.1178 ± 0.0012	$0.1170^{+0.0014}_{-0.0013}$	$0.11721^{+0.00093}_{-0.00091}$	0.1174 ± 0.0017
P_T	A priori non-grazing transit prob	...	$0.0791^{+0.0035}_{-0.0036}$	0.0790 ± 0.0037	$0.0785^{+0.0032}_{-0.0035}$...
$P_{T,G}$	A priori transit prob	...	$0.1021^{+0.0046}_{-0.0047}$	0.1019 ± 0.0048	$0.1013^{+0.0042}_{-0.0045}$...
F_0	Baseline flux	...	1.00018 ± 0.00016	1.00001 ± 0.00016	1.00009 ± 0.00011	...
Secondary Eclipse Parameters:						
T_S^f	Time of eclipse (BJD _{TDB})	...	$5200.611^{+0.016}_{-0.014}$	$5200.611^{+0.016}_{-0.014}$	$5200.611^{+0.016}_{-0.014}$	5178.698 ± 0.027
b_S	Impact parameter	...	$0.351^{+0.062}_{-0.088}$	$0.366^{+0.071}_{-0.10}$	$0.331^{+0.057}_{-0.076}$...
$T_{S,FWHM}$	FWHM duration (days)	...	$0.0989^{+0.0034}_{-0.0039}$	$0.0980^{+0.0034}_{-0.0037}$	$0.0988^{+0.0033}_{-0.0040}$...
τ_S	Ingress/egress duration (days)	...	$0.0144^{+0.0011}_{-0.0010}$	$0.0144^{+0.0013}_{-0.0012}$	$0.01409^{+0.00096}_{-0.00091}$	0.0154 ± 0.0018
$T_{S,14}$	Total duration (days)	...	$0.1134^{+0.0038}_{-0.0045}$	$0.1125^{+0.0038}_{-0.0044}$	$0.1130^{+0.0037}_{-0.0046}$	0.1137 ± 0.0060
P_S	A priori non-grazing eclipse prob	...	$0.0828^{+0.0026}_{-0.0027}$	$0.0829^{+0.0032}_{-0.0031}$	0.0820 ± 0.0021	...
$P_{S,G}$	A priori eclipse prob	...	$0.1070^{+0.0036}_{-0.0037}$	$0.1070^{+0.0044}_{-0.0043}$	0.1058 ± 0.0029	...

^a Priors for the transit fitting are available at <http://exoplanets.org/csv-files/exoplanets.csv>.

^b ‘...’ indicates the parameter was not determined in the discovery work.

^c The agreement between ‘All LCs + RVs’ and the discovery work (Quinn et al. 2012) is calculated.

^d For R band, $u_1=0.432^{+0.017}_{-0.016}$, $u_2=0.2461^{+0.0095}_{-0.0100}$; for V band, $u_1=0.542 \pm 0.020$, $0.206^{+0.013}_{-0.014}$.

^e For R band, $u_1=0.437^{+0.017}_{-0.016}$, $u_2=0.2433^{+0.0094}_{-0.010}$; for $Sloani$ band, $u_1=0.365 \pm 0.014$, $u_2=0.2519^{+0.0072}_{-0.0073}$; for V band, $u_1=0.548 \pm 0.020$, $u_2=0.202 \pm 0.014$.

^f For clarity, T_S are given in the form of BJD_{TDB}-2450000.

Table 4. Values of R_P/R_* for each of the filter data

Passband	R_P/R_*	R_P/R_* of All LCs + RVs agreement(σ) ^a	
V	0.1270 ± 0.0021		0.04
Sloani	0.1269 ± 0.0015	$0.1269^{+0.0011}_{-0.0016}$	0.00
R	$0.1278^{+0.0022}_{-0.0019}$		0.41

^aThe agreement between ‘All LCs + RVs’ and each filter data is calculated.

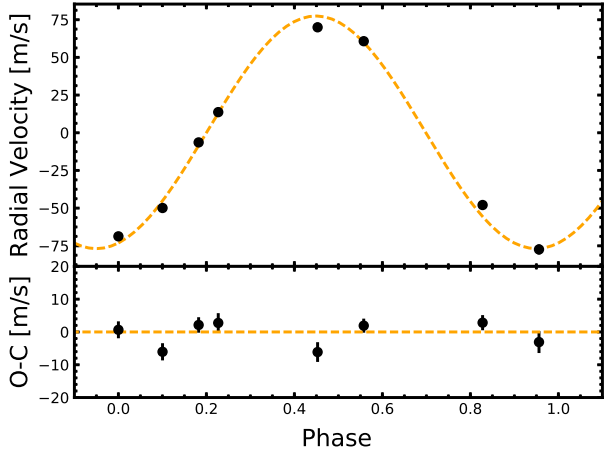


Figure 3. Keck/HIRES RV measurements of HAT-P-25 from Quinn et al. (2012), along with the best-fit model from the joint modeling of RVs and light curves. The best-fit is plotted as dashed orange line. The O-C residuals are displayed on the bottom panel, which has a RMS scatter $\sigma = 3.89 m s^{-1}$.

4.3. Orbital stability and mass-limit of a nearby perturber

Our timing study allows us to place an upper mass-limit on hypothetical perturbing planets located on orbits either interior or exterior to the orbit of the transiting planet. This technique is a potentially promising method to detect additional companions in a known transiting system (Agol et al. 2005; Holman & Murray 2005; Nesvorný & Morbidelli 2008). Upper mass-limit determinations are accomplished via numerical orbit integrations as has previously been done by several studies (Hoyer et al. 2011, 2012; Wang Y. et al. 2017). We have modified the Fortran-based MECHANIC (Słonina et al. 2015) orbital integration package to detect and accurately calculate transit events in the presence of a selected perturbing planet. This is done via a series of iterative back-and-forth integrations once the transiting

planet passes the face of the host star. The integrator⁵ is based on an extrapolation-algorithm adopting the explicit midpoint rule. Automatic step-size control and order selection are key features that permit this algorithm to be both robust and accurate. Integration control parameters were set slightly above the machine precision for maximum accuracy (at the expense of computing time). The MECHANIC package utilizes OpenMPI⁶ allowing the simultaneous spawning of hundreds of parallel integrations. We took advantage of the availability of computing power and chose a direct brute-force (but highly robust) approach, in calculating root-mean-square statistics for numerical transit timing data. Within the framework of the three-body problem we integrated the equations of motion and recorded the transit number and time in the event of a transit by iteration. In these calculations we used both the best-fit radii of the planet and its host star. This generated a series of mid-transit times to which we found an analytic least-squares fit enabling the calculation of the RMS statistic. We have tested this procedure by reproducing the TTV signal shown by Figure 1 in Nesvorný & Morbidelli (2008). The difference between TTV signals in Nesvorný & Morbidelli (2008) and in our code test is on a 1-second level or below. This test was also carried out previously and additional information on the calculation of TTVs is given in Hinse et al. (2015). This is done on a grid of masses and semi-major axes for the perturbing planet. At the same time (same grid point) we calculated the MEGNO factor (Cincotta & Simó 2000; Goździewski et al. 2001; Cincotta et al. 2003; Hinse et al. 2010) during the integration. MEGNO provides information on the degree of chaos present in the system. A MEGNO close to 2 indicates quasi-periodic (usually regular) behavior while values substantially larger than 2 indicate chaos, which is often accompanied by large-scale orbital instabilities. The MEGNO technique’s main advantage is the localization of orbital mean-motion resonances, and we utilize this advantage in the present work.

Our results are shown in Figure 5 to Figure 7. We explored the range $0.1 < P_2/P_1 < 3.65$ in orbital period ratio by fixing the osculating elements of the transiting planet to its best-fit values and allowing the perturbing planet to start in the interval from 0.02 to 0.10 AU. The mass range of the perturber was probed from 0.1 to $1000 M_{\oplus}$. In the figures, we show the resulting MEGNO with the perturber mass-limit function super-

⁵ odex.f: <http://www.unige.ch/~hairer/prog/nonstiff/odex.f>

⁶ <http://www.open-mpi.org/>

Table 5. Mid-transit times for HAT-P25b as determined from JKTEBOP (see sec. 3)

Epoch Number	T_C (BJD _{TDB})	σ (second)	O-C (second)
-351	2455136.671678	68.88	2.70
-334	2455198.769490	32.83	-2.08
39	2456561.268725	57.43	-90.84
45	2456583.187731	90.75	91.60
54	2456616.062365	91.74	30.50
57	2456627.021282	50.77	71.33
175	2457058.050613	103.43	-181.80
270	2457405.069613	108.43	-51.25
273	2457416.029497	154.05	72.91
350	2457697.295638	56.30	15.10

imposed (corresponding to the 80 seconds as obtained from our timing analysis). Timing variation signals with a larger (smaller) RMS scatter will be shifted upward (downward) (Hoyer et al. 2011). We mark the location of orbital resonances by vertical arrows. Furthermore, in each panel, we study the effect of various initial conditions of the perturbing planet on the overall dynamics and the resulting mass-limit function. In general, we see that the system becomes unstable/chaotic for configurations where the two planets are in close proximity to each other, and where the interactions are thus strongest. The calculation of the RMS statistic proves more difficult when the two bodies interact strongly, which can generate inclination perturbations that destroy transit regularity. As a consequence, for such cases, numerical data is sparse.

Considering exterior orbits, we can conclude that the upper mass-limit of a perturber in the 3:1 orbital resonance is around $0.5 M_{\oplus}$, and for the 2:1 resonance, the limit is somewhat smaller at around $0.3 M_{\oplus}$. The mass-limit for a perturber in the 7:2 or 5:2 resonance is strongly dependent on the initial conditions. For interior orbits, a perturber of a maximum of $0.5 M_{\oplus}$ in the 1:2 resonance would produce a TTV signal with a root-mean-square of 80s for nearly all initial conditions. The upper mass-limit at the 3:1 resonance depends on the initial conditions, as can be seen from the figures. In the case of co-planar orbits and sufficient photometric precision, however, an interior perturber would potentially have revealed itself by a transit signal. In between all low-order resonances (exterior as well as interior) we detect higher-order resonances at which one could potentially detect the presence of a relatively low mass planets.

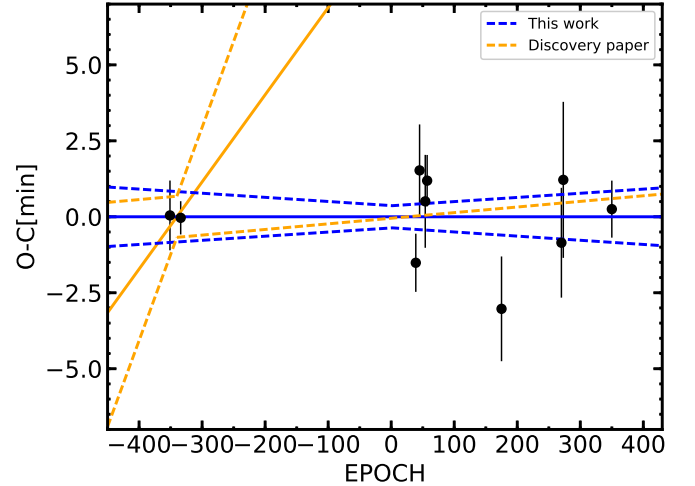


Figure 4. Observed minus calculated mid-transit times for HAT-P-25b. Adopting the updated linear ephemeris, transit timing residuals calculated with all transit epochs are shown. The first two mid-transit times are from Quinn et al. (2012), and others belong to this work. The solid blue line represents zero deviation from the predicted time of transit. The blue dashed line represents the propagation of $\pm 1\sigma$ errors associated with the calculated orbital period. Based on the linear ephemeris calculated using the two transit light curves from Quinn et al. (2012), a solid yellow line and dash yellow lines are plotted. These show the effect of using the imperfectly determined period.

4.4. The light travel time effect and the mass-limit of a long-term perturber

In §4.3, we discussed the TTVs caused by the gravitational interactions between the transiting planet and a perturber. This, however, is not the only source of TTVs. The interaction between planet and perturber becomes weaker when the distance between them becomes longer. For large period ratios, the movement of the host stellar barycenter caused by the perturber becomes the dominant source of TTVs. This is known as the light travel time effect (TTV_{LTTE}; Irwin 1952; Irwin 1959), and is calculated by:

$$\text{TTV}_{\text{LTTE}} = \frac{(G)^{1/3} P^{2/3} (1-e^2) m_p \sin(i)}{c(2\pi)^{2/3} (m_* + m_p)^{2/3}} \frac{\sin(\omega + f[t])}{1 + e \cos(f[t])} \quad (2)$$

where the true anomaly, f , is the function of time, ω is the argument of the periastron, e is the eccentricity, i is the inclination, and m_* is the mass of the HAT-P-25 host star, m_p is the mass of the perturber, c is the speed of light, and G is the gravitational constant.

As described in §4.2, the TTVs we observed do not show significant timing variations, and have an RMS of only ~ 80 s. This limits the upper mass of the hy-

Table 6. Limits on Nearby Stars for HAT-P-25

band	Limiting for Annulus Centered at...					Ref
	74 AU	148 AU	297 AU	597 AU	1188 AU	
<i>Ks</i> (Δmag^a)	...	1.88	4.27	6.79	7.78	Adams et al. (2013)
<i>Sloanz</i> (Δmag^a)	3.80	4.27	5.57	5.80	...	Wöllert & Brandner (2015)
upper mass-limits ^b (M_J)	...	568.22	201.98	69.41	27.37	

^a E.g., an object with $\Delta\text{mag} = 5$ near a star with magnitude = 12 is assigned a magnitude of 17.

^b Based on *Ks* magnitude, we calculated the upper mass-limits of nearby stars at the specified distance.

pothetical perturber according to TTV_{LTTE} (Montalto 2010). We calculated this upper mass for every hypothetical semi-major axis and TTV RMS. We then created a heat map as shown in Figure 8. The curve of RMS of $\text{TTV}_{\text{LTTE}} = 80\text{s}$ is highlighted in red. Planets of lower mass than delimited by this curve are not excluded from the system by our observations.

For our calculation, we assumed that the orbits of the transiting planet and the perturber are circular and coplanar, implying that e is 0, ω is 0, and i is 90° , thereby giving a conservative estimate of the upper mass-limit of long-term perturbers.

In parallel, the lack of a significant trend in the RVs (e.g., Wright et al. 2007; Knutson et al. 2014) provides an opportunity to determine an independent upper mass-limit on hypothetical perturbers through the radial velocity reflex velocity relation

$$\text{RV} = K[\cos(f[t] + \omega) + e\cos\omega], \quad (3)$$

where K is the radial velocity semi-amplitude which is calculated by

$$K = \left(\frac{2\pi G}{P(m_* + m_p)^2}\right)^{1/3} \frac{m_2 \sin i}{\sqrt{1-e^2}}. \quad (4)$$

The curve of the upper mass-limit from the analysis of RVs is highlighted in blue in the Figure 8.

According to our calculations, the limit from the analysis of RVs is more sensitive when the semi-major axis is short (shorter than 6.25 AU in this case). On the contrary, the limit from the analysis of TTVs is effective as the semi-major axis exceeds 6.25 AU. Synthesizing the analysis of the RMS of TTVs and the RVs, the upper mass-limit of perturbing stellar companion in the distance of 0 to 11.17 AU is 3000 M_J .

Moreover, there are two observations (Adams et al. 2013; Wöllert & Brandner 2015) of high spatial resolution for this system. In these works, they put the magnitude limits on the nearby stars around HAT-P-25. Hence, we can calculate the mass-limits on the

nearby stars according to the relation of absolute magnitude in *Ks* and stellar mass (Pecaut & Mamajek 2013). Based on the magnitude limits given in Adams et al. (2013) and Wöllert & Brandner (2015), we obtained the upper mass-limits for HAT-P-25's nearby stars by linearly interpolating the mass-magnitude relation given by Pecaut & Mamajek (2013). The magnitude limits and upper mass-limits are listed in Table 6.

5. DISCUSSION AND CONCLUSION

Between Nov 2013 and Nov 2016, we obtained eight transit light curves of the hot Jupiter HAT-P-25b, which quintuples the number of literature transits available for this system to date. Based on the analysis of our new photometric data, along with two follow-up light curves and RV data obtained from discovery work (Quinn et al. 2012), we presented new estimates of the system parameters for HAT-P-25, which is consistent with those in discovery work. Moreover, we significantly improved linear ephemeris ($T_{C[0]} = 2456418.80996 \pm 0.00025$ [BJD_{TDB}] and $P = 3.65281572 \pm 0.00000095$ days); our improved orbital period is 1.78s shorter than previous one reported in discovery work.

The analysis of TTV_G allowed us to place an upper mass-limit of a hypothetical nearby perturbing planet as a function of its orbital separation. Near the 1:2, 2:1, and 3:1 resonances with HAT-P-25b, a perturber with mass greater than 0.5, 0.3 and 0.5 M_\oplus can be excluded, respectively. The mass-limit for a perturber in the 1:3, 5:2, and 7:2 resonance are strongly dependent on the initial conditions. Moreover, the analysis of TTV_{LTTE} allowed us to present the upper mass-limit of the long-term perturber. A long-term perturber with mass greater than 3000 M_J within 11 AU of the star can be excluded.

One might struggle to counter the argument that the results of the current paper are mundane. Our analysis reinforces the conclusion that the HAT-P-25

system fits into the well-worn hot Jupiter narrative (Winn & Fabrycky 2015b). A short-period Jupiter-like planet, bereft of any detectable companions, orbits an otherwise unremarkable sun-like star at a distance far inside the radius at which the core accretion process (Pollack et al. 1996) is conventionally held to operate.

Our view is that follow-up observations of the type reported here are important. Some of the most illuminating insights gained from the exoplanets have flowed from the rare hot Jupiters that turn out to have companions. For example, the outer worlds orbiting Upsilon Andromedae (Butler et al. 1999) provided the first opportunity to investigate the effects of large-scale, potentially dissipation-free orbital instability (Ford et al. 2005). The HAT-P-13 system (Bakos et al. 2009) produced an entirely unanticipated invitation to probe the interior structure of a planet beyond the solar system (Batygin et al. 2009; Buhler et al. 2016). More recently, the WASP-47 system (Hellier et al. 2012), with its paradigm-confounding architecture (Becker et al. 2015) has offered an abundance of clues to how planetary systems form and evolve.

In the context of the forthcoming NASA’s TESS and ESO’s GAIA mission, more meaningful researches can be conducted with TEMP: 1). More precise estimate of a upper mass of long-term perturber can be given through the mutual verification of the TTV_{LTTE} and the astrometric measurement performed by GAIA. 2). The masses of nearby perturbers (especially near resonance perturbers), however, can only be effectively constrained by the TTV_{G} , because astrometric technique is not sensitive to this type of perturbers. 3). Most importantly, time baseline for typical TESS field is only about 27 days while the period of typical TTV_{G} signal is several years. Hence, the high-precision photometric follow-up observations are required to perform decisive TTV analysis.

Over the past decade, a number of best practices for ground-based transit follow-up have emerged, spanning differential photometry, precise time handling, and Bayesian model selection. As outlined in this paper, we have incorporated these developments into our procedures. Given the unique longitude of our facilities, and our consistent access to meter+ class telescopes, we are confident that our systematic approach will allow us to eventually add to the list of landmark multiple-planet systems that contain hot Jupiters.

6. ACKNOWLEDGEMENT

S.W. thanks the Heising-Simons Foundation for their generous support.

This research was supported by the National Natural Science Foundation of China and the Chinese Academy of Sciences Joint Fund on Astronomy (No. U1431105); the Key Development Program of Basic Research of China (No. 2013CB834900); the National Basic Research Program of China (Nos. 2014CB845704, and 2013CB834902); the National Natural Science Foundation of China (No. 11333002, 11373033, 11433005, 11673027, 11403107, 11503009, 11673011); the Young Scholars Program of Shandong University, Weihai (No. 2016WHWLJH07); the Natural Science Foundation of Jiangsu Province (BK20141045); the National Defense Science and Engineering Bureau civil spaceflight advanced research project (D030201); the KASI grant 2016-1-832-01 and 2017-1-830-03. Results from numerical simulations were partly performed by using a high performance computing cluster at the Korea Astronomy and Space Science Institute.

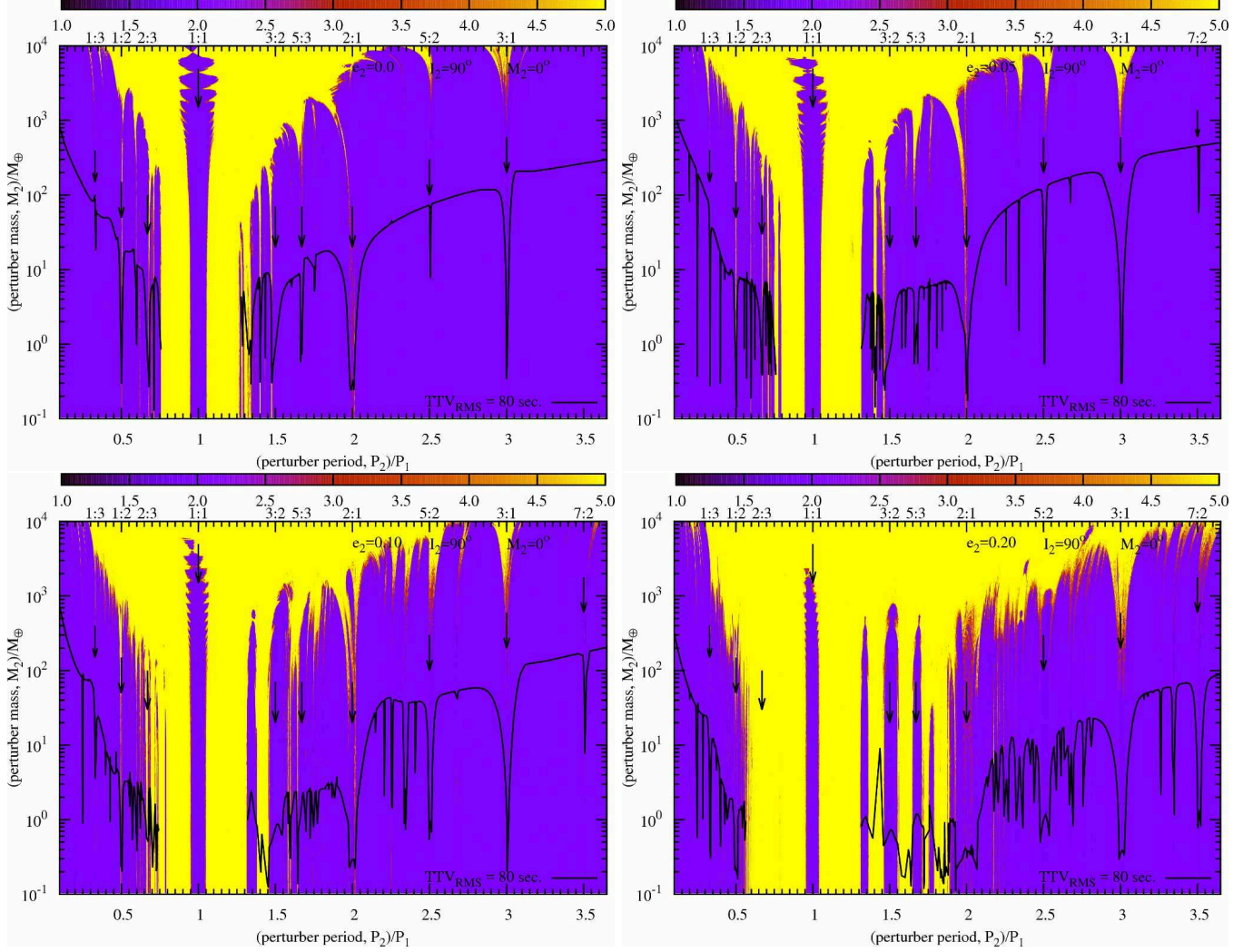


Figure 5. MEGNO stability maps superimposed on an upper mass-limit function of a hypothetical perturber. A MEGNO of around 2 indicates quasi-periodic (regular) orbits. A MEGNO of 5 or larger indicates strongly chaotic (unstable) behavior. The colors refer to final MEGNO values after each grid integration, see text for details. For larger eccentricities of the perturber, the region around the transiting planet becomes increasingly chaotic (unstable). Vertical arrows indicate the location of (P_2/P_1) orbital resonances between the transiting planet and a perturber. The black line represents mass-period parameters for which the perturber introduces a TTV signal with a root-mean-square of 80 seconds as determined by our timing analysis. Each panel explores a survey in different initial eccentricity of the perturber ranging from circular to 0.20. In all maps the pair (ω_2, Ω_2) was set to zero initially. *A color version of this figure is available in the electronic version of this manuscript.*

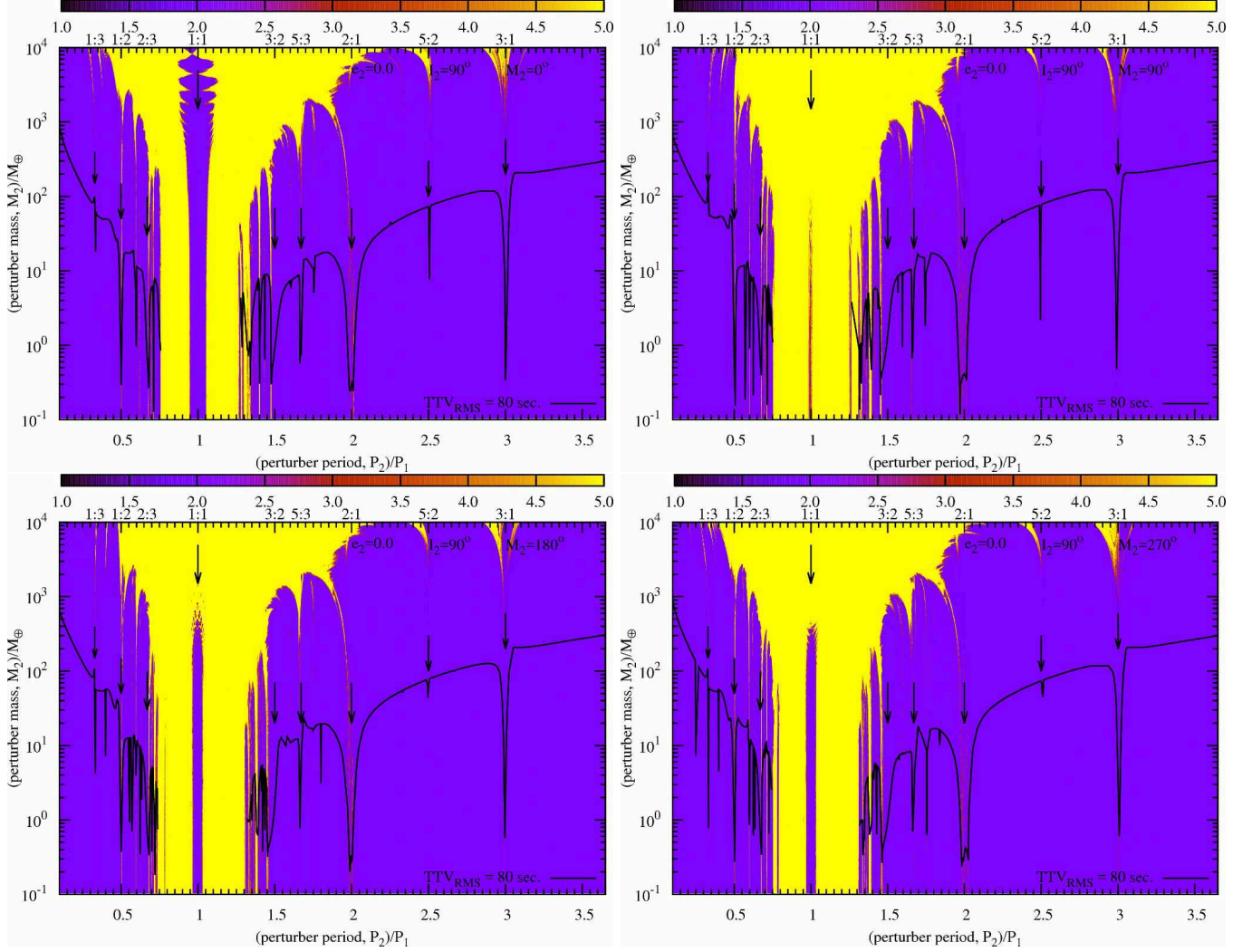


Figure 6. Same as fig. 5, but this time exploring different initial mean anomalies of the perturbing planet. Qualitatively, the quasi-periodic central co-orbital 1:1 resonance now ceases significance and is replaced by general chaos (mainly for $M_2 = 90^\circ$). A color version of this figure is available in the electronic version of this manuscript.

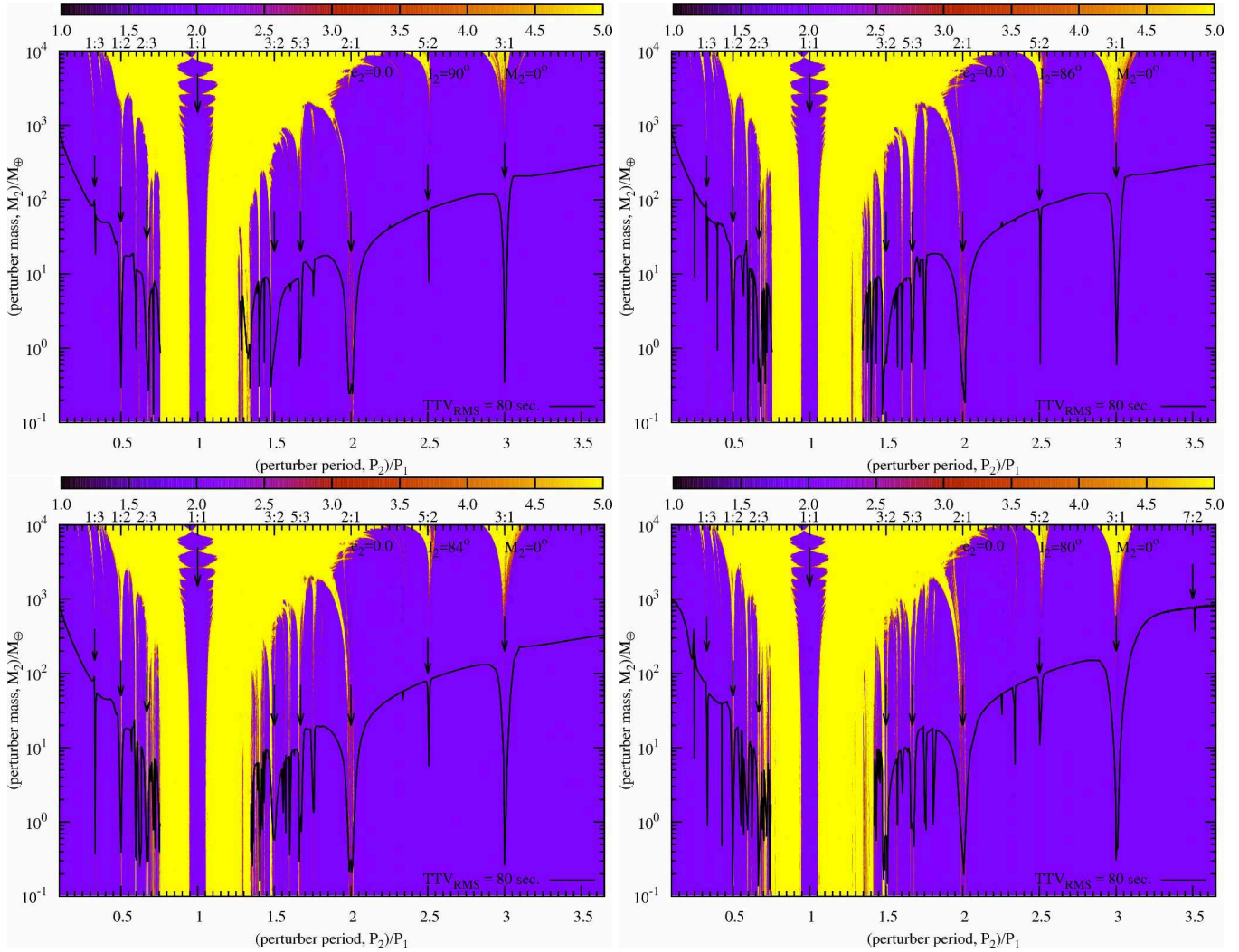


Figure 7. Same as fig. 5, but this time exploring different initial orbital inclinations of the perturbing planet. Qualitatively, the effect of varying the perturbing planet’s inclination is small. *A color version of this figure is available in the electronic version of this manuscript.*

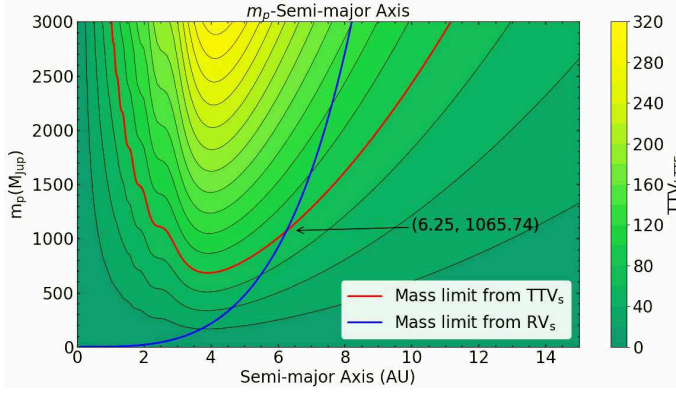


Figure 8. Contours of RMSs of TTVs, the curve of the TTVs' RMS of 80s and the RMS of 3.86s curve of the residual of the best-fit RVs, with RMS in color scale. The black solid contours mark the value of the RMS across the m_p -Semi-major Axis space. The red curve and the blue curve represent the upper mass-limit derived from the analysis of TTVs and the analysis of RVs respectively.

REFERENCES

- Adams, E. R., Dupree, A. K., Kulesa, C., & McCarthy, D. 2013, *AJ*, 146, 9
- Addison, B. C., Tinney, C. G., Wright, D. J., et al. 2014, ArXiv e-prints, arXiv:1403.0652
- Agol, E., Steffen, J., Sari, R., & Clarkson, W. 2005, *MNRAS*, 359, 567
- Bakos, G. Á., Howard, A. W., Noyes, R. W., et al. 2009, *ApJ*, 707, 446
- Batygin, K., Bodenheimer, P., & Laughlin, G. 2009, *ApJL*, 704, L49
- Batygin, K., Bodenheimer, P. H., & Laughlin, G. P. 2016, *ApJ*, 829, 114
- Becker, J. C., Vanderburg, A., Adams, F. C., Rappaport, S. A., & Schwengeler, H. M. 2015, *ApJL*, 812, L18
- Bertin, E., & Arnouts, S. 1996, *A&AS*, 117, 393
- Buhler, P. B., Knutson, H. A., Batygin, K., et al. 2016, *ApJ*, 821, 26
- Butler, R. P., Marcy, G. W., Fischer, D. A., et al. 1999, *ApJ*, 526, 916
- Cincotta, P. M., Giordano, C. M., & Simó, C. 2003, *Physica D Nonlinear Phenomena*, 182, 151
- Cincotta, P. M., & Simó, C. 2000, *A&AS*, 147, 205
- Collins, K. A., Kielkopf, J. F., & Stassun, K. G. 2017, *AJ*, 153, 78
- Eastman, J., Gaudi, B. S., & Agol, E. 2013, *PASP*, 125, 83
- Eastman, J., Siverd, R., & Gaudi, B. S. 2010, *PASP*, 122, 935
- Ford, E. B., Lystad, V., & Rasio, F. A. 2005, *Nature*, 434, 873
- Goździewski, K., Bois, E., Maciejewski, A. J., & Kiseleva-Eggleton, L. 2001, *A&A*, 378, 569
- Hellier, C., Anderson, D. R., Collier Cameron, A., et al. 2012, *MNRAS*, 426, 739
- Hinse, T. C., Christou, A. A., Alvarelos, J. L. A., & Goździewski, K. 2010, *MNRAS*, 404, 837
- Hinse, T. C., Haghighipour, N., Kostov, V. B., & Goździewski, K. 2015, *ApJ*, 799, 88
- Holman, M. J., & Murray, N. W. 2005, *Science*, 307, 1288
- Hoyer, S., Rojo, P., & López-Morales, M. 2012, *ApJ*, 748, 22
- Hoyer, S., Rojo, P., López-Morales, M., et al. 2011, *ApJ*, 733, 53
- Hu, S.-M., Han, S.-H., Guo, D.-F., & Du, J.-J. 2014, *Research in Astronomy and Astrophysics*, 14, 719
- Huang, C., Wu, Y., & Triaud, A. H. M. J. 2016, *ApJ*, 825, 98
- Irwin, J. B. 1952, *ApJ*, 116, 211
- . 1959, *AJ*, 64, 149
- Knutson, H. A., Fulton, B. J., Montet, B. T., et al. 2014, *ApJ*, 785, 126
- Montalto, M. 2010, *A&A*, 521, A60
- Nesvorný, D., & Morbidelli, A. 2008, *ApJ*, 688, 636
- Pecaut, M. J., & Mamajek, E. E. 2013, *ApJS*, 208, 9
- Pollack, J. B., Hubickyj, O., Bodenheimer, P., et al. 1996, *Icarus*, 124, 62
- Queloz, D., Eggenberger, A., Mayor, M., et al. 2000, *A&A*, 359, L13
- Quinn, S. N., Bakos, G. Á., Hartman, J., et al. 2012, *ApJ*, 745, 80
- Sing, D. K., Fortney, J. J., Nikolov, N., et al. 2016, *Nature*, 529, 59
- Słonina, M., Goździewski, K., & Migaszewski, C. 2015, *NewA*, 34, 98
- Southworth, J., Maxted, P. F. L., & Smalley, B. 2004a, *MNRAS*, 349, 547
- . 2004b, *MNRAS*, 351, 1277
- Steffen, J. H., Ragozzine, D., Fabrycky, D. C., et al. 2012, *Proceedings of the National Academy of Science*, 109, 7982
- ter Braak, C. J. F. 2006, *Statistics and Computing*, 16, 239
- Torres, G., Winn, J. N., & Holman, M. J. 2008, *ApJ*, 677, 1324
- Wang, S., Addison, B., Fischer, D. A., et al. 2018a, *AJ*, 155, 70
- Wang, S., Wu, D.-H., Addison, B. C., et al. 2018b, *AJ*, 155, 73
- Wang Y., H., Wang, S., Liu, H.-G., et al. 2017, *AJ*, 154, 49
- Winn, J. N., & Fabrycky, D. C. 2015a, *ARA&A*, 53, 409
- . 2015b, *ARA&A*, 53, 409
- Winn, J. N., Noyes, R. W., Holman, M. J., et al. 2005, *ApJ*, 631, 1215
- Wöllert, M., & Brandner, W. 2015, *A&A*, 579, A129
- Wright, J. T., Marcy, G. W., Fischer, D. A., et al. 2007, *ApJ*, 657, 533
- Yang, Y.-G. 2009, *PASJ*, 61, 1211
- Zhou, X., Chen, J., Xu, W., et al. 1999, *PASP*, 111, 909